Draft version, January 11, 2017
Preprint typeset using LaTeX style emulateapj v. 5/2/11

arXiv:1702.00195v1 [astro-ph.GA] 1 Feb 2017

CHEMICAL CARTOGRAPHY. I. A CARBONICITY MAP OF THE GALACTIC HALO

Young Sun Lee[1], Timothy C. Beers[2], Young Kwang Kim[1], Vinicius Placco[2], Jinmi Yoon[2], Daniela Carollo[3,4], Thomas Masseron[5], and Jaehun Jung[6]

Draft version, January 11, 2017

ABSTRACT

We present the first map of carbonicity, [C/Fe], for the halo system of the Milky Way, based on a sample of over 100,000 main-sequence turnoff stars with available spectroscopy from the Sloan Digital Sky Survey. This map, which explores distances up to 15 kpc from the Sun, reveals clear evidence for the dual nature of the Galactic halo, based on the spatial distribution of stellar carbonicity. The metallicity distribution functions of stars in the inner- and outer-halo regions of the carbonicity map reproduce those previously argued to arise from contributions of the inner- and outer-halo populations, with peaks at [Fe/H] = −1.5 and −2.2, respectively. From consideration of the absolute carbon abundances for our sample, A(C), we also confirm that the carbon-enhanced metal-poor (CEMP) stars in the outer-halo region exhibit a higher frequency of CEMP-no stars (those with no overabundances of heavy neutron-capture elements) than of CEMP-*s* stars (those with strong overabundances of elements associated with the *s*-process), whereas the stars in the inner-halo region exhibit a higher frequency of CEMP-*s* stars. We argue that the contrast in the behavior of the CEMP-no and CEMP-*s* fractions in these regions arises from differences in the mass distributions of the mini-halos from which the stars of the inner- and outer-halo populations formed, which gives rise in turn to the observed dichotomy of the Galactic halo.

Subject headings: Methods: data analysis — technique: imaging spectroscopy — Galaxy: halo — stars: abundances — stars: carbon

1. INTRODUCTION

Observations of the kinematics and chemistry of stars in the halo of the Milky Way (MW) provide valuable clues to its assembly history, and that of other large galaxies in general. Until relatively recently, the MW's diffuse stellar halo has been thought to comprise only a single stellar population – stars with similar ages, chemical abundances, and kinematics. This long-standing idea has been challenged in the past decade by both observations (e.g., Carollo et al. 2007, 2010; de Jong et al. 2010; Beers et al. 2012; An et al. 2013, 2015; Hattori et al. 2013; Allende Prieto et al. 2014; Chen et al. 2014; Fernandez-Alvar et al. 2015, 2016a, 2017; Janesh et al. 2016; Das & Binney 2016) and ever more sophisticated simulations of the formation of large MW-like galaxies (e.g., Zolotov et al. 2009; Font et al. 2011; McCarthy et al. 2012; Tissera et al. 2013, 2014). We briefly summarize our current understanding below.

1.1. *The Nature of the Galactic Halo*

The evidence presented to date indicates that the diffuse Galactic halo comprises at least two distinct stellar components – the inner-halo population (IHP) and the outer-halo population (OHP), which can be distinguished based on their different spatial distributions, metallicity ([Fe/H][7]), and kinematics. As summarized by Carollo et al. (2010) and Beers et al. (2012), the inner-halo component dominates the population of halo stars found at distances up to 10–15 kpc from the Galactic center, while the outer-halo component dominates in the region beyond 15–20 kpc. In addition, the inner halo exhibits a flatter density profile than the nearly spherical outer halo. The metallicity distribution function (MDF) of inner-halo stars peaks at [Fe/H] = –1.6, while the outer-halo stars exhibit a peak at [Fe/H] = –2.2. Kinematically, the IHP shows either zero or slightly prograde rotation with respect to the Galactic center, with stars on somewhat eccentric orbits, while the OHP exhibits a net retrograde rotation of about –80 km s^{-1}, with stars on more circular orbits (Carollo et al. 2007, 2010; Kinman et al. 2012; Hattori et al. 2013). The observed velocity ellipsoids of the populations also differ, in the sense that the OHP is kinematically "hotter" than the IHP (Carollo et al. 2007, 2010, 2014; An et al. 2015; Helmi et al. 2017).

This view has been challenged by claims that systematic errors in adopted distances may artificially induce an apparent dual nature of the halo for samples whose kinematics are deduced from relatively local stars (Schönrich et al. 2011). However, Beers et al. (2012) refuted this argument, based on a number of lines of evidence. Furthermore, Das & Binney (2016), using a completely different modeling approach for distant K-type giants from the Sloan Digital Sky Survey (SDSS; York et al. 2000), come to essentially the same conclusions as those arising from

[1] Department of Astronomy and Space Science, Chungnam National University, Daejeon 34134, Korea; youngsun@cnu.ac.kr
[2] Department of Physics and JINA Center for the Evolution of the Elements, University of Notre Dame, Notre Dame, IN 46556, USA
[3] Research School of Astronomy and Astrophysics, The Australian National University, Canberra, ACT 2611, Australia
[4] INAF–Osservatorio Astronomico di Torino, Strada Osservatorio 20, Pino Torinese, I-10020, Italy
[5] Institute of Astronomy, University of Cambridge, Madingley Road, Cambridge CB3 0HA, UK
[6] Department of Astronomy, Space Science, and Geology, Chungnam National University, Daejeon 34134, Korea

[7] We use the terms metallicity and [Fe/H] interchangeably throughout this paper.

the interpretation of the local kinematics of halo stars. Most recently, Helmi et al. (2017) have used parallaxes and proper motions from the first Gaia data release (Gaia Collaboration et al. 2016), in combination with metallicity estimates from Data Release 5 of the RAVE survey (Kunder et al. 2016), to provide confirming evidence that the retrograde signature for OHP stars is highly unlikely to be an artifact of incorrect distance estimates in previous work.

Claims that the selection function of metal-poor stars in local samples may have led to an incorrect dual-halo inference (echoed by, e.g., Monachesi et al. 2016) have been empirically resolved by the results of An et al. (2013, 2015). These authors estimated metallicities from coadded SDSS *ugriz* photometry for stars with distances in the range 5–10 kpc from the Sun, and derived an MDF with two peaks (one at [Fe/H] ~ -1.4 and the other at [Fe/H] ~ -1.9). They associated the more metal-rich component with the IHP and the more metal-poor component with the OHP. They further demonstrated that the two populations exhibit the expected kinematic signatures inferred from the analysis of Carollo et al. (2007, 2010). Since no spectroscopic selection is made in the analysis by An et al., the argument that the dual-halo interpretation could arise from such a source is rendered moot.

1.2. *Carbon-enhanced Metal-poor Stars as Probes of the Galactic Halo System*

Among the stars of the halo system, the so-called carbon-enhanced metal-poor (CEMP; Beers & Christlieb 2005) stars have emerged as important tracers of the assembly and star-formation history of the Galactic halo, as summarized briefly here.

It has been recognized for over a decade that CEMP stars can be divided into several subclasses, according to their level of neutron-capture element enhancement – CEMP-no, CEMP-s, CEMP-r, and CEMP-r/s (Beers & Christlieb 2005). CEMP-no stars exhibit no overabundances of heavy neutron-capture elements, while CEMP-s objects show strong overabundances of elements associated with the s-process, such as Ba. CEMP-r stars possess strong enhancements of r-process elements such as Eu. Carbon-enhanced stars with possible contributions from both the r-process and the s-process have been classified as CEMP-r/s stars[8].

The ever-growing numbers of CEMP stars with available high-resolution spectroscopic results have shown that the CEMP-s and CEMP-no stars are the most populous subclasses, accounting for more than 95% of the samples of carbon-enhanced stars at low metallicity. Numerous studies have also shown that the frequency of CEMP stars in the halo system dramatically increases with decreasing metallicity (e.g., Lucatello et al. 2006; Lee et al. 2013; Yong et al. 2013; Placco et al. 2014), as well as with distance from the Galactic plane (Frebel et al. 2006; Carollo et al. 2012; Beers et al. 2016). It has also become clear that most CEMP-no stars have [Fe/H] < -2.5, while CEMP-s stars are predominantly found among with [Fe/H] > -2.5 (e.g., Aoki et al. 2007; Yoon et al. 2016). Long-term radial-velocity monitoring of CEMP stars (e.g., Starkenburg et al. 2014; Hansen et al. 2016a,b; Jorissen et al. 2016) has provided strong evidence for different binary fractions associated with the CEMP-s and CEMP-no stars – $\sim$82% of CEMP-s (including CEMP-r/s) stars are binaries, while **only** $\sim$17% of CEMP-no stars are binaries, consistent with the observed binary fraction of other metal-poor stars in the halo (Carney et al. 2003). It is thus clear that binarism is not required to account for the origin of the CEMP-no stars; their distinctive chemical signatures are very likely the result of the pollution of their natal clouds by first-generation stars.

From a kinematic analysis of CEMP stars in SDSS, Carollo et al. (2012) reported a higher fraction of CEMP stars associated with the OHP than with the IHP. From a similar analysis of the limited number of stars with available high-resolution spectroscopic classifications of CEMP stars, Carollo et al. (2014) demonstrated that the OHP exhibits a relatively higher fraction of CEMP-no stars than found for CEMP stars associated with the IHP, which slightly favored CEMP-s stars over CEMP-no stars.

The goal of this study is twofold. We first explore further evidence for the dichotomy of the diffuse halo system, based on the observed *in situ* spatial distribution of a large sample of $\sim$ 105,700 main-sequence turnoff (MSTO) stars from SDSS with measured carbon-to-iron ratios ([C/Fe], which we refer to as "carbonicity"), located within 15 kpc of the Sun. Secondly, we search for the origin of the duality of the Galactic halo by assessing the relative fractions of CEMP-no and CEMP-s stars in the chemically separated IHP and OHP, making use of a recently suggested scheme based on absolute carbon abundances, A(C)[9], developed by Yoon et al. (2016), to distinguish CEMP-no stars from CEMP-s stars based on medium-resolution spectroscopy alone. Note, however, that our MSTO sample covers substantially different ranges in metallicity and luminosity than the sample of Yoon et al. (2016). Yoon et al.'s sample is dominated by metal-poor giants with [Fe/H] < -2.0, while our MSTO stars primarily cover [Fe/H] > -2.5. As is addressed in Section 4.4, these different samples suggest we must apply different reference points of the critical A(C) value to separate CEMP-no from CEMP-s stars than that (A(C) = 7.1) of Yoon et al. (2016).

This paper is arranged as follows. Section 2 summarizes the criteria used to select our program stars. In Section 3, we validate our measurement of [C/Fe] by comparison with available high-resolution spectroscopy and noise-added synthetic spectra. In Section 4, we obtain the spatial distribution of [C/Fe] for the stars in our sample, and identify four regions that we associate with different stellar populations in the MW. The MDFs and the carbonicity distribution functions (CDFs) for each region are considered. We also assess the fractions of the CEMP-no stars and CEMP-s stars for these regions. Section 5 presents a plausible origin of the dichotomy of the Galactic halo, based on the data in hand. A summary of our results, and prospects for future work, is presented in Section 6.

[8] Recently, Hampel et al. (2016) have presented compelling evidence that the CEMP-r/s stars are more likely associated with a proposed intermediate neutron-capture process, the i-process.

[9] The conventional notation is used, $A(\mathrm{C}) = \log\epsilon(\mathrm{C}) = \log(N_{\mathrm{C}}/N_{\mathrm{H}}) + 12$.

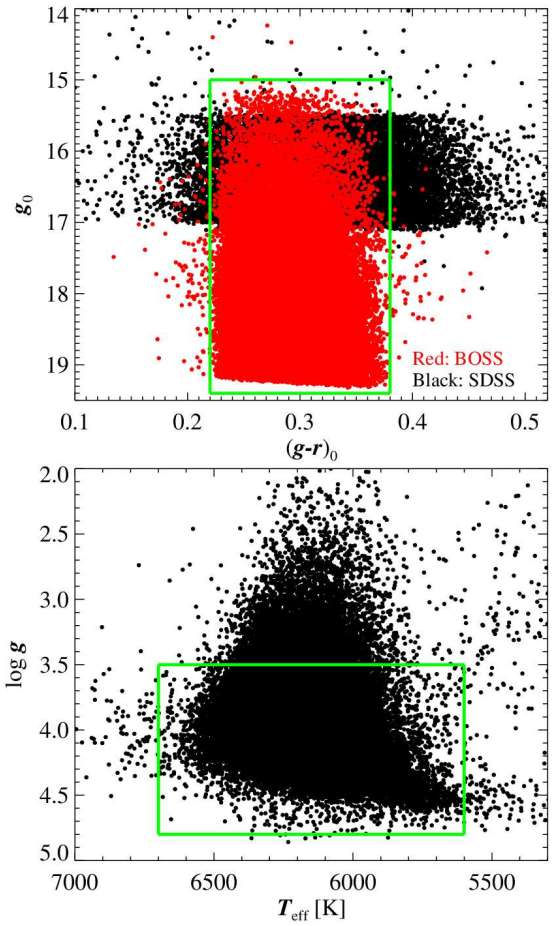


Figure 1. Distribution of g_0 vs. $(g-r)_0$ (top panel) and log g vs. $T_{\rm eff}$ (bottom panel) for spectrophotometric standard stars from SDSS. The red dots represent stars from BOSS, while the black dots are stars from legacy SDSS, SEGUE-1, and SEGUE-2. The green boxes in the top and bottom panels indicate the magnitude and color cuts and the surface gravity and temperature cuts used to select our sample stars, respectively. Note that only spectrophotometric standard stars are shown in this figure; our final selected sample comprises all stars from the legacy SDSS, SEGUE-1, SEGUE-2, and BOSS surveys that satisfy these criteria.

2. SAMPLE SELECTION

The sample used in this study primarily comprises medium-resolution ($R \sim 2000$) spectra for stars observed during the course of the legacy SDSS program and the Sloan Extension for Galactic Understanding and Exploration (SEGUE-1; Yanny et al. 2009), as well as SEGUE-2 (C. Rockosi et al. 2017, in preparation). We also included spectra of spectrophotometric standard stars obtained during the Baryon Oscillation Spectroscopic Survey (BOSS; Dawson et al. 2013), which was one of the four projects executed during the third phase of the SDSS (Alam et al. 2015).

We selected stellar spectra from legacy SDSS, SEGUE-1, SEGUE-2, and BOSS, based on g_0 magnitude, $(g-r)_0$ color, surface gravity (log g), and effective temperature ($T_{\rm eff}$) that satisfied the following conditions: $15.0 \leq g_0 \leq 19.4$, $0.22 \leq (g-r)_0 \leq 0.38$, $3.5 \leq \log\ g \leq 4.8$, and $5600\ {\rm K} \leq T_{\rm eff} \leq 6700\ {\rm K}$. The magnitude and color cuts are similar to those for the selection of spectrophotometric standard stars in BOSS, which correspond to the MSTO objects of an old stellar population; the gravity and temperature ranges also restrict our sample to MSTO stars. The green boxes in Figure 1 indicate the ranges of magnitude, color, surface gravity, and temperature used to select our program stars.

Estimates of the stellar atmospheric parameters ($T_{\rm eff}$, log g, and [Fe/H]) for our program stars were obtained through application of the SEGUE Stellar Parameter Pipeline (SSPP; Lee et al. 2008a,b; Allende Prieto et al. 2008; Lee et al. 2011; Smolinski et al. 2011). The carbonicity, [C/Fe], was estimated following the procedures of Lee et al. (2013). Typical errors in the stellar parameters are ~ 180 K for $T_{\rm eff}$, ~ 0.24 dex for log g, and ~ 0.23 dex for [Fe/H], respectively, while the error in the estimated [C/Fe] is better than 0.35 dex in the temperature range $4400\ {\rm K} \leq T_{\rm eff} \leq 6700$ K for spectra with signal-to-noise ratios ${\rm S/N} \geq 15\ {\rm Å}^{-1}$ (Lee et al. 2013), increasing to ~ 0.5 dex at ${\rm S/N} = 10\ {\rm Å}^{-1}$. More recent tests of errors in the SSPP estimates of carbonicity suggest that these estimates are conservative, and that the actual errors in their determination are likely to be ∼0.25–0.35 dex over these ranges in S/N.

We removed stars from our sample that were drawn from spectroscopic plug-plates taken in the direction of open cluster and globular cluster fields, in order to minimize contamination. Since there are many stars that were observed more than once, we chose to include only the spectrum with the highest S/N for multiply observed stars. We visually inspected all the spectra of stars with [Fe/H] ≤ –1.0 used in our program to exclude cool white dwarfs and objects with defects in their spectra, which could lead to spurious estimates of atmospheric parameters. For a clear detection of the CH G-band around 4300 Å, which ensures a good measurement of [C/Fe], we selected spectra for stars with equivalent widths of the carbon feature in the region 4290–4318 Å larger than 0.6 Å, because we have found that spurious estimates of [C/Fe] become significant below this value.

We followed the methodology of Beers et al. (2000, 2012) to determine the distance to each star; the typical distance uncertainty is of the order of 15-20%. This was then used to compute the distance from the Galactic mid-plane, Z, and the distance from the Galactic center projected onto the plane, R, assuming the Sun is located at 8.5 kpc from the Galactic center.

Our final sample comprises stars with spectra having ${\rm S/N} \geq 12\ {\rm Å}^{-1}$ (see the next section for justification of this cut) and valid estimates of $T_{\rm eff}$, log g, [Fe/H], [C/Fe], Z, and R. The total number of stars in the sample is $N \sim 105,700$.

3. CHECK ON ESTIMATE OF [C/FE] FOR WARM, METAL-POOR STARS

3.1. *Comparison with High-resolution Spectroscopy*

The BOSS calibration stars in our sample are extremely useful probes of the Galactic halo, because they reach two magnitudes fainter than the legacy SDSS and SEGUE calibration stars (see Figure 1). Although inclusion of redder stars would add a large number of more distant giants, one clear advantage of our MSTO sample is that stars in this stage of evolution do not suffer from dilution of their surface carbon abundances by material that has undergone CN cycling (due to extra mixing occurring along the red-giant branch).

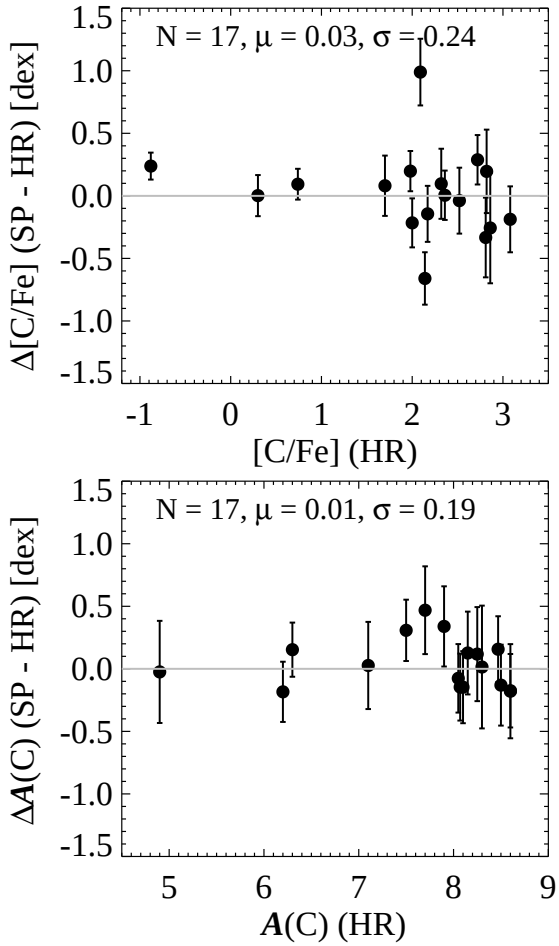


Figure 2. Distribution of residuals for SSPP-estimated [C/Fe] (top panel) and A(C) (bottom panel) as a function of the high-resolution determinations. 'SP' indicates the estimates from the SSPP; 'HR' refers to the literature values from Yoon et al. (2016). After correction for a +0.16 dex offset in the SSPP estimates (already performed for the data shown in the figure; see text), there are no significant trends in the residuals. The legend for each panel lists the total number of comparison stars (N), the mean offset (μ), and the standard deviation (σ). The error bars are calculated by adding the uncertainties of the SSPP and HR estimates in quadrature. We assumed that the typical uncertainty of the HR [C/Fe] determination is 0.1, and 0.2 dex for A(C). The uncertainty for the SSPP estimate is that provided by the pipeline.

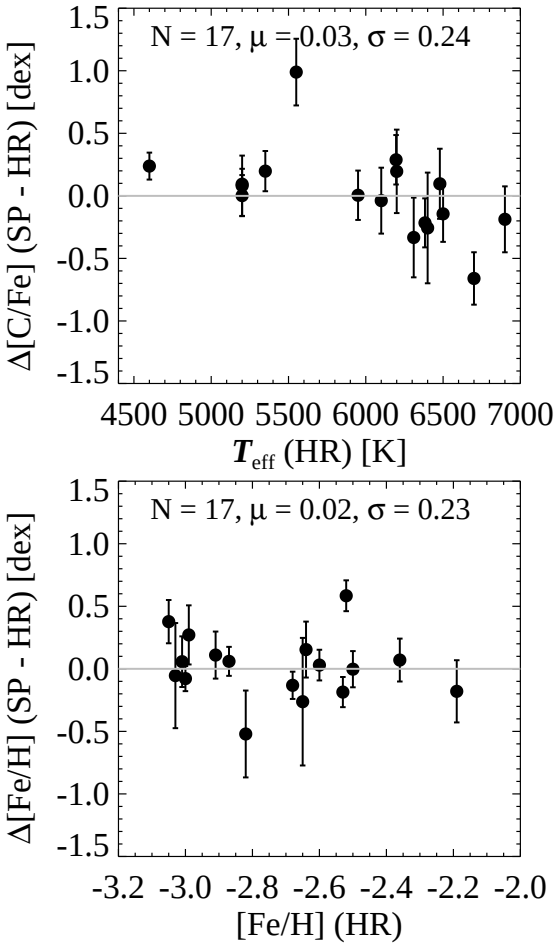


Figure 3. Top panel: Distribution of residuals for SSPP-estimated [C/Fe], as a function of $T_{\rm eff}$, after correction for the +0.16 dex offset in the SSPP estimates. 'SP' and 'HR' are as defined in Figure 2. No significant trend of the SSPP [C/Fe] residuals with $T_{\rm eff}$ is found. Bottom panel: Distribution of residuals for SSPP-estimated [Fe/H], as a function of the HR metallicity estimates; no corrections were needed with respect to the HR determinations. No trend with [Fe/H] is seen. The error bars are calculated by adding the uncertainties of the SSPP and HR estimates in quadrature. We assumed that the typical uncertainty of both HR [C/Fe] and HR [Fe/H] determinations is 0.1 dex. The uncertainty for the SSPP estimate is that provided by the pipeline.

We note, however, that this choice also introduces some difficulty for the detection of molecular carbon features for a subset of the MSTO stars in our sample, in particular for warmer and lower-metallicity stars. This follows because the strength of the CH G-band around 4300 Å, which is used by the SSPP to estimate [C/Fe], decreases at higher temperatures and lower metallicity. As a result, some bona-fide CEMP stars may escape detection, and will be misclassified as carbon-normal stars. This problem occurs even for high-resolution spectroscopic analyses – examples of such cases are the well-known warm, metal-poor subdwarfs G 64-12 ([Fe/H] = –3.29) and G 64-37 ([Fe/H] = –3.11), whose status as CEMP-no stars was only recently demonstrated by Placco et al. (2016), based on extremely high S/N ($\sim$ 700), high-resolution ($R \sim 95,000$) spectra.

In order to check the reliability of the SSPP estimate of carbonicity, we first compared our [C/Fe] values with the results from high-resolution spectroscopy for the small sample of stars in common from Table 1 of Yoon et al. (2016). Figure 2 shows the results of this exercise. The top panel of this figure is a residual plot of the SSPP-estimated [C/Fe] compared to the literature values, where 'SP' indicates the estimation from the SSPP, and 'HR' indicates the literature value from Yoon et al. (2016). We identified a positive offset between the SSPP and literature estimates of [C/Fe] of +0.16 dex, and have reduced the plotted SSPP carbonicity estimates by this amount. The bottom panel is a similar residual plot, but for A(C)[10]. The offset of +0.16 dex in [C/Fe] is also corrected in this panel.

The top panel of Figure 3 shows the distribution of the carbonicity residuals as a function of $T_{\rm eff}$ (corrected for

[10] A(C) = log ϵ(C) is obtained from the medium-resolution determinations using A(C) = [C/Fe] + [Fe/H] + A(C) $_\odot$, where we adopt the solar abundance of carbon from Asplund et al. (2009), $A(C)_\odot = 8.43$.

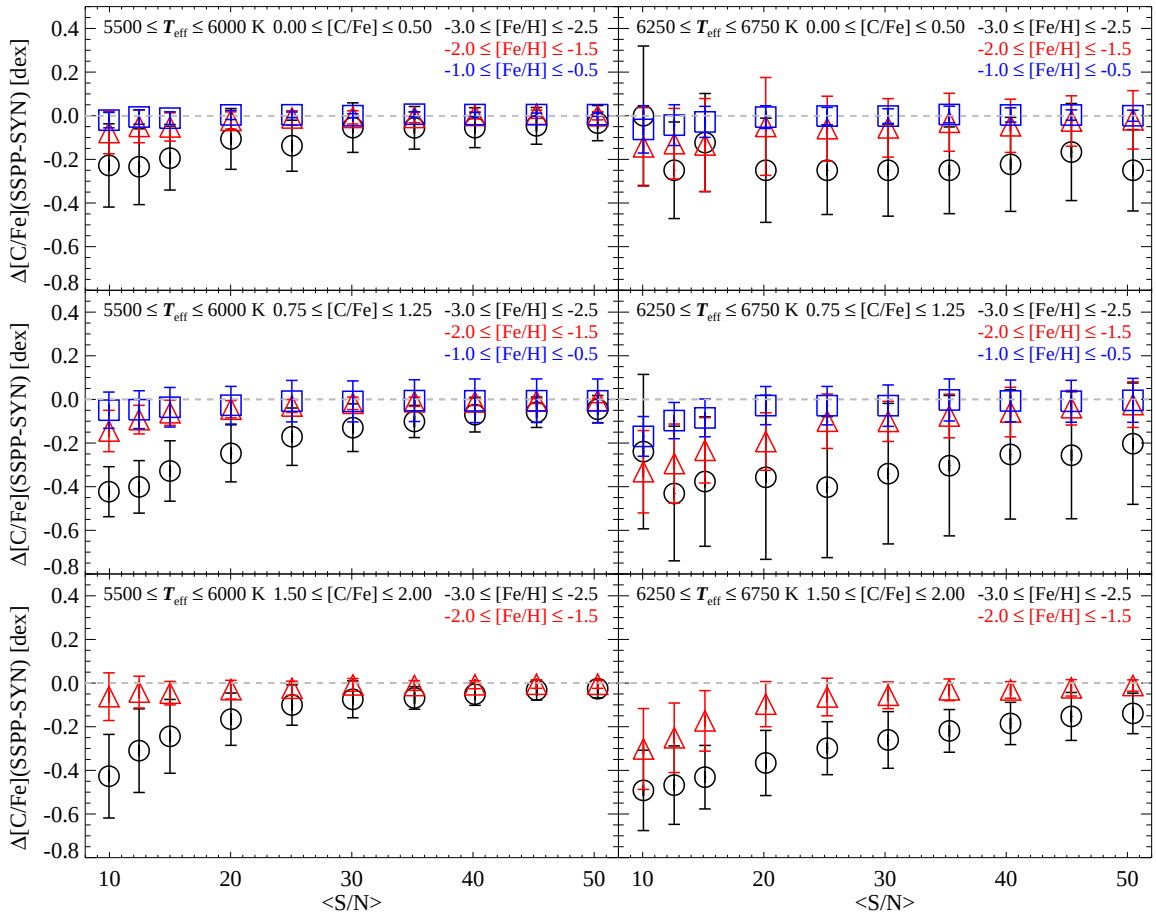


Figure 4. Distribution of residuals in [C/Fe] between the SSPP (denoted as 'SSPP') estimates and values obtained for noise-added synthetic spectra (indicated by 'SYN'). ⟨S/N⟩ is an average signal-to-noise ratio per angstrom. The ranges of $T_{\rm eff}$, [Fe/H], and [C/Fe] are listed in the legend of each panel. Each symbol is represented by the same color as the metallicity range. The error bar is represented by the standard deviation for the stars in each bin of S/N.

the +0.16 dex offset as before). The bottom panel is the distribution of metallicity residuals as a function of the HR literature estimates of [Fe/H]; we found no significant metallicity offset of the SSPP estimates from the high-resolution values. In summary, Figures 2 and 3 do not exhibit any significant trends of the SSPP [C/Fe] and [Fe/H] estimates against the high-resolution estimates, and show good agreement with very small scatter, even in the range of [Fe/H] < –2.5. Most of the comparison stars fall in the same warm, low-metallicity regime as for our sample stars; it appears that we are able to obtain reliable estimates of [C/Fe] using the SSPP for these stars.

3.2. *Impact of Signal-to-noise Ratio on [C/Fe]*

The difficulty of detecting molecular carbon features for warmer and lower-metallicity stars in our sample becomes worse for low-S/N spectra, and may also result in underestimates of [C/Fe], even when the carbon features are detected. Below we describe a set of tests we have carried out to quantify these effects.

We first injected noise into the grid of synthetic spectra that was used to estimate [C/Fe]. We then chose an SDSS/SEGUE spectrum that has similar values of $T_{\rm eff}$ and [Fe/H] to a model spectrum to which we want to add noise, and created a noise vector by dividing the flux of the model spectrum by the S/N values of the selected SDSS/SEGUE spectrum as a function of wavelength. Following this step, we injected the generated noise into the synthetic spectra and obtained noise-added synthetic spectra with S/N = 10.0, 12.5, 15.0, 20.0, 25.0, 30.0, 35.0, 40.0, and 50.0 Å^{-1}, and simulated 25 different noise-added synthetic spectra at each S/N value. Finally, we processed the noise-added spectra through the SSPP to determine estimates of [C/Fe], holding the $T_{\rm eff}$ and log g values that represent the synthetic spectra fixed, and letting only [Fe/H] and [C/Fe] vary (as is done for the usual operation of the SSPP on program stars) to minimize the χ^2 values.

We proceeded by grouping the noise-added synthetic spectra into two regions of $T_{\rm eff}$ (5500–6000 K and 6250–6750 K), three regions of [Fe/H] (–1.0 to –0.5, –2.0 to –1.5, and –3.0 to –2.5), and three regions of [C/Fe] (+0.00 to +0.50, +0.75 to +1.25, +1.50 to +2.00). We only considered one gravity range, 3.5 ≤ log g ≤ 4.5. These ranges of temperature, gravity, and metallicity well represent the parameter space of our MSTO sample. For each S/N value, we then obtained the median and standard deviation of the differences in [C/Fe] estimates between the SSPP-estimated values and the model values for each group of spectra. We adopted a median rather than a mean value to prevent the residuals from being dominated by a few spurious determinations of [C/Fe], especially for low-S/N spectra.

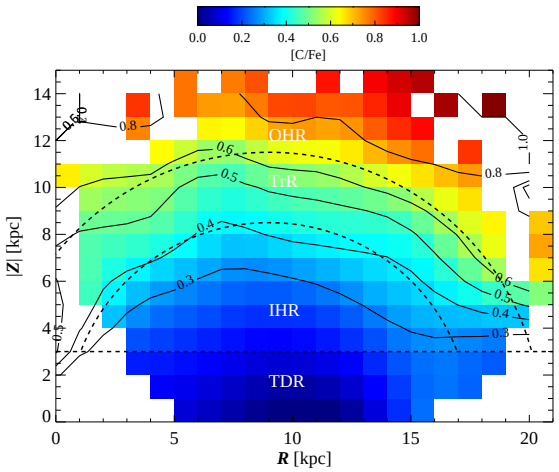


Figure 5. Map of carbonicity, [C/Fe], for our MSTO sample in the plane of $|Z|$ vs. R. $|Z|$ is the absolute distance from the Galactic mid-plane, while R is the distance from the Galactic center projected onto the plane, R. The bin size is 1×1 kpc; each pixel contains at least three stars. The color code is based on the median value of [C/Fe] in each pixel, with the color scale shown above the plot. Contours of median [C/Fe] values are overplotted. The dashed line at $|Z| = 3$ kpc indicates the approximate upper boundary of a thick-disk region (TDR), while the area between the upper limit of the thick disk and the inner dashed circle represents an inner-halo region (IHR). The area above the outer dashed circle is assigned to an outer-halo region (OHR). The area between the inner and outer dashed circles is associated with a transition region (TrR), where stars from both the IHP and OHP are expected to be found. Each region is abbreviated in white letters. We have applied a Gaussian kernel to the map to obtain a smooth distribution of [C/Fe]. We decided to force stars with [C/Fe] > +1.0 into the [C/Fe] = +1.0 bin, and stars with [C/Fe] < 0.0 into the [C/Fe] = 0.0 bin, in order to better illustrate the subtle contrast in the map.

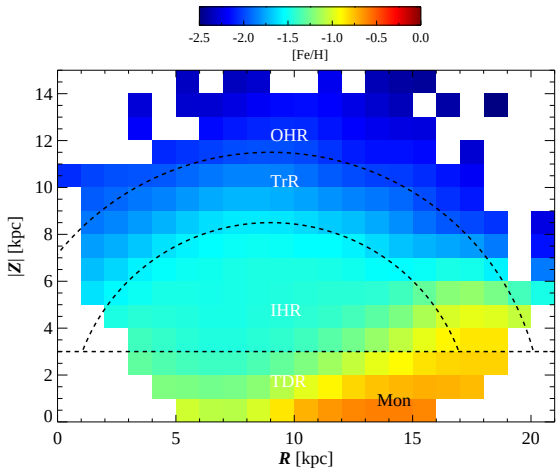


Figure 6. Same as in Figure 5, but for metallicity, [Fe/H]. It is clear that the regions (abbreviated in white letters) selected to demarcate the levels of carbonicity in Figure 5 also correspond to different levels of metallicity. Note, in particular, the contrast between the IHR, with [Fe/H] ∼ –1.5, and the OHR, with [Fe/H] < –2.0. We have applied a Gaussian kernel to the map to obtain a smooth distribution of [Fe/H]. We decided to force stars with [Fe/H] < –2.5 into the [Fe/H] = –2.5 bin, and stars with [Fe/H] > 0.0 into the [Fe/H] = 0.0 bin, in order to better illustrate the subtle contrast in the map. The Monoceros stream, with [Fe/H] ∼ –1.0, appears as a yellow-orange region at $R > 10$ kpc and $|Z| < 5$ kpc, and is labeled as "Mon".

Figure 4 shows how the residuals in [C/Fe] change with S/N. The ranges of temperature, metallicity, and carbonicity considered are listed at the top of each panel; the symbols have the same colors as the metallicity ranges. The label 'SSPP' indicates the SSPP values, whereas 'SYN' denotes the model values. In the figure, ⟨S/N⟩ is an average S/N per angstrom. The error bar represents the standard deviation.

Figure 4 indicates that our technique for determining [C/Fe] reproduces it reasonably well, because the median difference between the SSPP and the model is mostly less than 0.3 dex, commensurate with the uncertainty of the SSPP [C/Fe] estimate, for [Fe/H] ≥ –2.0 and S/N ≥ 12.5 Å^{-1}. Larger deviations exist for stars with –3.0 ≤ [Fe/H] ≤ –2.5 and/or S/N < 20. Based on inspection of Figure 4, we adjusted our estimate of [C/Fe] by 0.1 or 0.2 dex for stars in the following ranges:

- 5600 ≤ $T_{\rm eff}$ < 6100 K, –2.5 < [Fe/H] ≤ –2.0, 12.0 ≤ S/N ≤ 20.0 (+0.1 dex correction)
- 5600 ≤ $T_{\rm eff}$ < 6100 K, [Fe/H] ≤ –2.5, S/N ≥ 12.0 (+0.2 dex correction)
- 6100 ≤ $T_{\rm eff}$ ≤ 6700 K, –2.0 ≤ [Fe/H] ≤ –1.5, 12.0 ≤ S/N ≤ 20.0 (+0.1 dex correction)
- 6100 ≤ $T_{\rm eff}$ < 6700 K, [Fe/H] ≤ –2.5, S/N ≥ 12.0 (+0.2 dex correction)

The numbers of stars affected are is 468, 54, 6676, and 1461, respectively. Stars for which the molecular carbon features are not detected fall out of our sample and are no longer considered.

One unexpected trend, seen in the first and second panels of the right-hand column of plots (the warmest stars), is that the residuals for the lowest-metallicity stars suddenly decrease at S/N = 10.0, in contrast to the behavior at higher S/N. This may be caused by a very broad and poorly constrained distribution of χ^2 values at low S/N, high $T_{\rm eff}$, and low [Fe/H], which results in an unreliable estimate of [C/Fe]. For this reason we decided to cut our sample by requiring S/N ≥ 12.0. Using a much larger grid of noise-added synthetic spectra, we are currently developing a procedure to derive a smooth correction function of SSPP-derived [C/Fe] for MSTO objects that could suffer from this problem, as functions of S/N, $T_{\rm eff}$, [Fe/H], and [C/Fe] of the observed medium-resolution spectra.

4. RESULTS

Having prepared our MSTO sample as described above, and carried out a number of small corrections to our estimates of [C/Fe], we now consider the distribution of carbonicity (Sec. 4.1) and metallicity (Sec. 4.2). We then consider the apparent dichotomy of the halo system of the Galaxy in metallicity (Sec. 4.3) and in absolute carbon abundance, A(C) (Sec. 4.4), over distances extending to 15 kpc from the Sun.

4.1. *Spatial Distribution of Carbonicity, [C/Fe]*

Figure 5 is a map of [C/Fe] for our MSTO sample in the plane of $|Z|$ vs. R. From inspection, it is clear that, at a given R, the median [C/Fe] (indicated by the contour lines) gradually increases with increasing $|Z|$. The dashed circles in the figure are centered at $R = 9$ kpc, the inner circle having a radius of 8.5 kpc, while the outer circle has a radius of 11.5 kpc. The inner circle falls close to the contour of [C/Fe] = +0.4, whereas the outer circle

closely follows the contour with [C/Fe] = +0.6. Making use of these contour lines as fiducials to guide our choice, we divide the map into four primary regions, and associate stars in each region with an expected dominant stellar population as follows:

- Thick-disk region (TDR) – The region with $|Z| \leq 3.0$ kpc shown in the figure. Stars in this region are likely to be dominated by the thick-disk population (TDP).
- Inner-halo region (IHR) – The region corresponding to $|Z| > 3$ kpc and the inner dashed circle, which closely follows the [C/Fe] = +0.4 contour. Stars in this region are expected to be dominated by the IHP.
- Outer-halo region (OHR) – The region beyond the outer dashed circle. Stars in this region are expected to be dominated by the OHP.
- Transition region (TrR) – Defined as the region between the two dashed circles. Stars in this region are expected to be contributed by both the IHP and OHP; for convenience we refer to these stars as a transition population (TrP), although it is understood that this represents an overlap of the IHP and OHP, not a separate population.

We adopt the distance cut at $|Z| \leq 3$ kpc for the TDR by considering the scale heights of the thick disk and the metal-weak thick disk determined by Carollo et al. (2010). The boundaries for the IHR and OHR are determined by inspection of the carbonicity contours. We emphasize that our scheme to separate the stellar populations for the IHR and OHR (as well as the TrR) is *not* based on metallicity or kinematics, but relies solely on the level of [C/Fe] at a given location. These regions are shown with white labels in Figure 5.

4.2. *Spatial Distribution of Metallicity, [Fe/H]*

Figure 6 is a metallicity map of our program sample over the same range of $|Z|$ and R as shown in Figure 5. The regions identified in the carbonicity map are also labeled in this figure. From inspection, each of the carbonicity regions exhibits a different level of metallicity – the IHR with [Fe/H] $\sim$ –1.5, and the OHR with [Fe/H] $\lesssim$ –2.0, similar to the proposed divisions of the IHP and OHP obtained in the analysis of Carollo et al. (2007, 2010) on the basis of local kinematics (stars within 4 kpc of the Sun). Note that the Monoceros Stream (Newberg et al. 2002; Ivezić et al. 2008) is clearly identifiable in the figure, and appears as the yellow-orange region with [Fe/H] $\sim$ –1.0 at $10 < R < 20$ kpc and $|Z| < 5$ kpc.

4.3. *Dichotomy from the Metallicity Distribution Functions*

We now investigate the metallicity distributions of each region defined in Figure 5, to test whether we can identify distinct MDFs associated with the inner- and outer-halo populations.

Figure 7 shows the MDFs (left column of panels) and CDFs (right column of panels) for the TDR, IHR, TrR, and OHR. Note that, when selecting the stars in each region, in addition to the criteria described in Figure 5, we applied $|Z| > 3$ kpc for the IHR, $|Z| > 5$ kpc for the TrR, and $|Z| > 7$ kpc for the OHR, in order to minimize cross-contamination from stars in the different regions.

Inspection of the left column of panels in the figure clearly shows that the peak of the MDFs shifts to lower metallicity as we move from the IHR to the OHR (from the second to the fourth plot). The MDF of the TDR shows two peaks – one arising from the canonical thick-disk population at [Fe/H] $\sim$ –0.6, the other from the IHP at [Fe/H] $\sim$ –1.5. The MDF for stars in the IHR exhibits a well-defined distribution with a peak at [Fe/H] = –1.5, associated with the IHP. The MDF of the TrR appears to have a broad distribution, presumably due to the presence of overlapping contributions from the IHP and the OHP. Finally, the stars in the OHR exhibit a well-defined peak at [Fe/H] $\sim$ –2.2. associated with the OHP.

Our peak value of [Fe/H] = –1.5 for stars in the IHR, which we argue are likely associated with the IHP, is similar to that obtained by An et al. (2015) for the IHP, [Fe/H] = –1.4, while the peak we obtain for the OHR, [Fe/H] = –2.2, is somewhat lower than the [Fe/H] = –1.9 for the OHP found by An et al. (2015). Note that An et al. explored an *in situ* sample of main-sequence stars covering a similar distance range to our MSTO sample, but truncated beyond 10 kpc from the Sun. The difference in the metallicity peaks of the OHP between the two analyses likely arises due to the increasing lack of sensitivity of photometric metallicity techniques based on broadband *ugriz* for stars with [Fe/H] < -2.0. Even though the divisions of the regions we consider were made on the basis of carbonicity, the peaks of the MDFs for the dominant populations we associate with each region also agree very well with those inferred to exist from an analysis of local kinematics by Carollo et al. (2007, 2010). Reaching such similar conclusions from three very different approaches provides confidence in the reality of the dual-halo nature of the MW.

The panels in the left column in Figure 7 also demonstrate the clear advantage gained by using chemical-abundance ratios to distinguish one component from another. In these panels, the green, blue, and red curves represent individual MDFs evaluated from a simple two-component Gaussian mixture-model analysis. The blue distribution represents the IHP, while the red distribution is associated with the OHP. Note that the stars assigned to the IHP by this approach have almost no contribution from stars of the OHP, whereas the objects classified as the OHP have only a negligible contribution from the IHP. These results indicate that chemical-abundance ratios provide a more powerful discriminator for the identification of stellar populations than the kinematic and orbital information (including angular momentum and integrals of motion) alone, which can result in substantial overlap of the populations.

The right column of panels in Figure 7 shows the CDF for each region. The number of stars in each panel is the same as in the corresponding panel on the left. Inspection of these panels indicates that the fraction of stars with carbon enhancements relative to iron clearly varies from region to region. The fiducial dashed lines indicate the solar [C/Fe] and the level of carbon enhancement conventionally used to identify CEMP stars, [C/Fe] $\geq +0.7$.

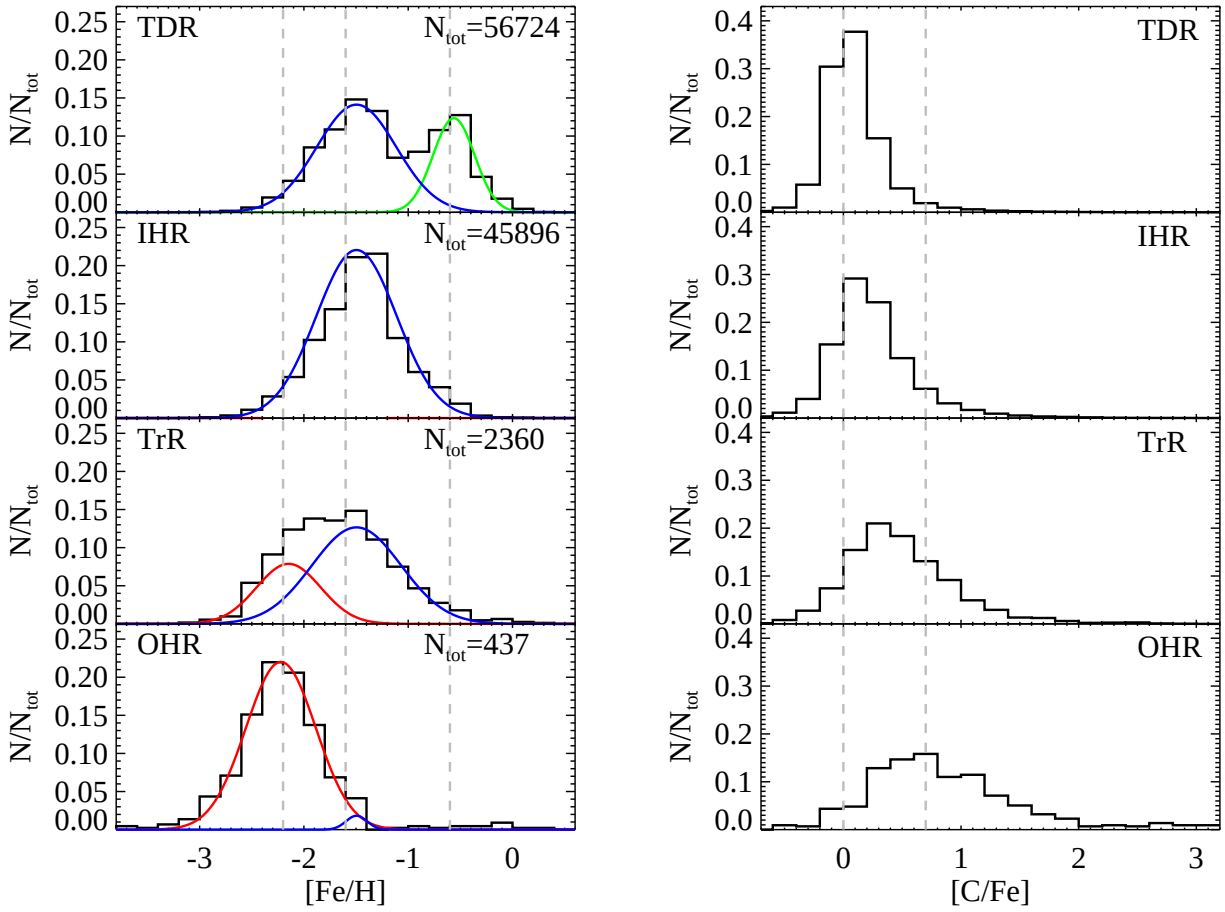


Figure 7. Histograms of the normalized fractions of metallicities ([Fe/H], left panels) and carbonicities ([C/Fe], right panels) in the four regions we have identified (see text). The labels TDR, IHR, TrR, and OHR represent the thick-disk region, the inner-halo region, the transition region, and the outer-halo region, respectively, defined on the basis of Figure 5. The total number ($N_{\rm tot}$) of stars for each region is listed in each panel. The vertical dashed lines in the left panels represent the mean metallicity of the canonical thick disk, [Fe/H] = –0.6, the IHP, [Fe/H] = –1.6, and the OHP, [Fe/H] = –2.2, according to Carollo et al. (2007, 2010). Gaussians derived from a simple mixture-model analysis are shown in blue for the IHP, red for the OHP, and green for the canonical TDP. The two vertical lines in the right panels denote the solar [C/Fe] and [C/Fe] = +0.7. The total number of stars in each region shown in the right panels is the same as in the left panels.

The fraction of CEMP stars increases as one proceeds from the TDR to the IHR, TrR, and OHR. This provides suggestive, but not yet definitive, evidence that different progenitors may be responsible for the majority production of carbon in the underlying stellar populations we associate with these regions.

4.4. *Dichotomy from Distribution of Absolute Carbon Abundances, A(C)*

The diversity of the heavy-element abundance patterns found among CEMP stars (CEMP-no, CEMP-*s*, CEMP-*r*, and CEMP-*r*/*s*) already indicates that there is likely to be more than one source of carbon production at low metallicity, and perhaps even within the subclasses themselves (see the discussion by Yoon et al. 2016). This, along with the contrast seen in the carbonicity map of the halo-system stars, suggests that different subclasses of CEMP stars might be associated with different dominant nucleosynthesis pathways within their associated stellar populations.

Carollo et al. (2014) tested this idea using the limited number of CEMP stars with high-resolution measurements of [C/Fe] and [Ba/Fe] then available to calculate the relative fractions of CEMP-*s* and CEMP-no stars associated with the IHP and OHP, separated on the basis of their integrals of motion. These authors demonstrated that the CEMP stars associated with the OHP exhibit a higher fraction (by about a factor of two) of CEMP-no stars than CEMP-*s* stars, while the IHP only slightly favors CEMP-*s* stars over CEMP-no stars. A much larger sample of CEMP stars is required, however, for confirmation of this behavior.

According to the conventional criterion used to distinguish CEMP-*s* stars from CEMP-no stars, a high-resolution spectroscopic measurement of (at least) the [Ba/Fe] ratio is required. However, Yoon et al. (2016) have recently developed a new method for separation of these subclasses of CEMP stars based solely on the absolute carbon abundance, A(C), which can be obtained from medium-resolution spectroscopy such as that available for our SDSS program stars. According to the classification exercise carried out by Yoon et al. (2016), CEMP-*s* stars have $A(\mathrm{C}) > 7.1$, while the CEMP-no stars have $A(\mathrm{C}) \leq 7.1$. We consider this approach to test whether or not the relative fractions of CEMP-no and CEMP-*s* stars in the OHR differ significantly from those in the IHR, and by inference, between the OHP and the IHP.

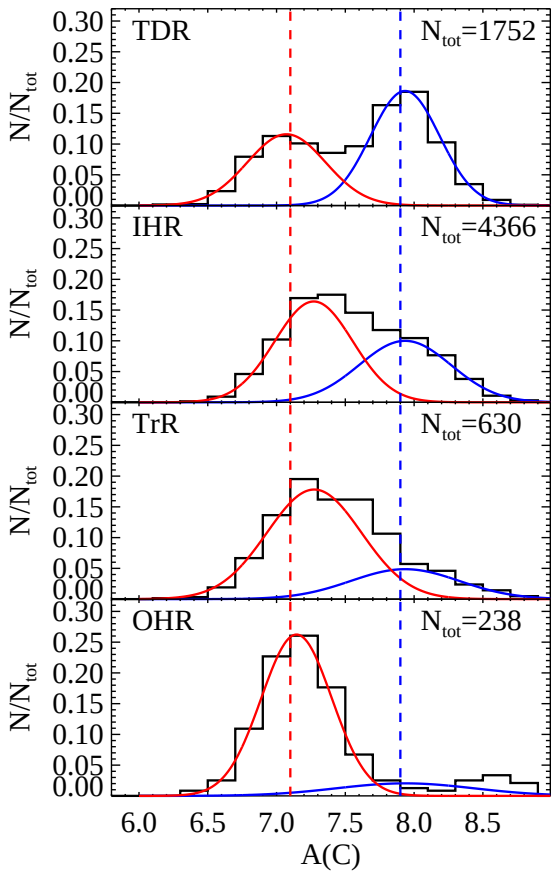


Figure 8. Histograms of the normalized fractions of absolute carbon abundances, A(C), for stars with [Fe/H] ≤ -1.0 and [C/Fe] $\geq +0.7$. The blue dashed vertical line represents the mean A(C) of the stars that Yoon et al. (2016) classify as CEMP-s, while the red dashed vertical line is the reference line to distinguish between the CEMP-no and CEMP-s stars used in Yoon et al. (2016). The notation for TDR, IHR, TrR, and OHR is the same as in Figure 7. Gaussians for a simple mixture-model analysis of the CEMP stars are shown in blue for the high-A(C) stars and red for the low-A(C) stars. The total number ($N_{\rm tot}$) of stars used to make the histogram is listed in each plot.

Figure 8 shows the distribution of A(C) for each region of the carbonicity map in Figure 5. To compare the two different subclasses of CEMP stars, we include only the stars with [C/Fe] $\geq +0.7$ and [Fe/H] ≤ -1.0 in the figure. The blue and red curves are Gaussians obtained from a simple two-sample mixture model for each region. The blue dashed vertical line represents the mean A(C) of the stars that Yoon et al. classify as CEMP-s, while the red dashed vertical line is the reference line to distinguish between the CEMP-no and CEMP-s stars used by Yoon et al. (2016). From inspection of this figure, the IHR exhibits a very broad distribution with likely separable peaks at A(C) ~ 7.3 and A(C) ~ 7.9, respectively, while the OHR exhibits a strong peak at A(C) $= 7.1$ and only a very small peak at A(C) ~ 7.9. Inspection of the A(C) distribution in the TrR shows the expected shift between these two different behaviors, because the relative proportion of the low-A(C) stars increases as one moves from the IHR to the OHR.

Quantitatively, if we separate stars in each region at A(C) $= 7.1$, the dividing line between CEMP-no and CEMP-s according to Yoon et al. (2016), we obtain fractions of 84% and 16% for high-A(C) and low-A(C) stars in the IHR, 77% and 23% in the TrR, and 63% and 37% in the OHR, respectively. On the other hand, using the fractions of high- and low-A(C) stars identified by the Gaussian mixture model for each region, we obtain 42% for the high-A(C) stars (blue curve in the figure) and 58% for the low-A(C) stars (red curve in the figure) in the IHR, 24% and 76% in the TrR, and 13% and 87% in the OHP, respectively. These results clearly indicate an increasing trend in the relative fractions of the low-A(C) stars with respect to the high-A(C) stars from the IHR to the OHR. The increasing fraction of low-A(C) stars provides strong suggestive evidence that different progenitors contributed to stellar populations we associate with these regions.

Unlike the mean value of A(C) $= 6.3$ for the low-A(C) stars found by Yoon et al. (2016), represented by CEMP-no stars (classifications based on high-resolution spectroscopy for a sample that included numerous giants), our distribution of low-A(C) stars exhibits a peak around A(C) $= 7.1$. This is *not* primarily because of our inability to detect low-A(C) CEMP-no stars in our sample of metal-poor MSTO stars, *but rather* because the stars in our program sample cover substantially different ranges of metallicity and luminosity. As shown in Figure 1 of Yoon et al. (2016), which we refer to as the Yoon–Beers diagram, their CEMP-no stars are dominated by objects with [Fe/H] < -3.0. On the other hand, as seen from Figure 7, our sample of MSTO stars is dominated by objects with [Fe/H] > -2.5. The Yoon–Beers diagram of Yoon et al. (2016) reveals that most of the CEMP-no stars in this metallicity range have A(C) > 6.3. If we consider only the CEMP-no stars with [Fe/H] > -3.0 from their sample, we obtain a peak for the low-A(C) stars at A(C) ~ 6.6. Moreover, excluding the giants with log g < 3.5 in the sample of Yoon et al. (2016), which are not present in our sample, we obtain a low-A(C) peak value of A(C) $= 6.8$. These two values are much closer to our determinations. The high-A(C) stars from Yoon et al., which include more objects with [Fe/H] > -2.5, have a mean value of A(C) $= 7.9$, in excellent agreement with our peak value of A(C) ~ 7.9, shown by the blue curve in Figure 8.

This exercise raises two important points. First, the appropriate A(C) division line between CEMP-s and CEMP-no stars may depend, at least weakly, on stellar temperature and luminosity class, and secondly, the the peak value of A(C) for CEMP-no stars varies over the metallicity range considered in a given sample. A value of A(C) ~ 7.6 would be a more suitable location to divide the low- and high- A(C) stars for our MSTO sample, rather than the level of A(C) $= 7.1$ for the sample of the Yoon et al., which included substantial numbers of cooler stars and more metal-poor stars.

5. IMPLICATIONS FOR THE ORIGIN OF THE DUALITY IN THE GALACTIC HALO SYSTEM

As discussed above, when the halo populations of the MW are separated based on their carbonicity, [C/Fe], we find that the component associated with the IHP exhibits a peak metallicity at [Fe/H] ~ -1.5, while the peak metallicity associated with the OHP is [Fe/H] ~ -2.2. These results are completely consistent with previous studies by Carollo et al. (2007, 2010) and An et al. (2013, 2015). We have also quantitatively assessed the fraction of CEMP-

no and CEMP-*s* stars in the OHP and IHP, classified on the basis of their observed A(C), and found that the stars associated with the OHP exhibit a higher proportion of CEMP-no stars, compared to CEMP-*s* stars, than found for stars associated with the IHP. These results suggest that the progenitors of these two classes of CEMP stars contributed to the outer- and inner-halo populations in different proportions, a valuable clue to unraveling the apparently different assembly histories of the OHP and IHP.

Current simulations of the hierarchical assembly of MW-like galaxies within the Λ-CDM paradigm (e.g., Tissera et al. 2012, 2013, 2014) show that the inner halo formed through mergers of a few relatively massive gas-rich mini-halos, which underwent dissipative (angular-momentum-conserving) collapse, in contrast with the stars of the outer halo, which formed in numerous lower-mass mini-halos that were accreted into the Galactic halo through chaotic, dissipationless mergers. In such a scenario, star formation in the relatively massive gas-rich subfragments that led to the inner halo would be expected to be very efficient, and chemical enrichment could proceed rapidly. This would lead to the formation of moderately metal-poor stars with [Fe/H] $\sim$ –1.5, including numerous intermediate-mass ($\sim$ 1–4 $M_{\odot}$) asymptotic giant branch (AGB) stars, a subset of which formed as members of the binaries that produced (via mass transfer of their nucleosynthesis products) the CEMP-*s* stars observed today. CEMP-no stars would have formed from the nucleosynthesis products of more massive progenitors during the first, or at least early, bursts of star formation in their parent mini-halos; some might also be expected to be present among early-generation stars in the mini-halos associated with the IHP. In this manner, one might understand the preferential production of CEMP-no stars at low metallicity, relative to CEMP-*s* stars, as reported by previous studies (e.g., Aoki et al. 2007; Placco et al. 2014; Yoon et al. 2016), as well as our present work.

The CEMP-no and CEMP-*s* stars are thought to originate from different classes of astrophysical progenitors: (1) CEMP-no stars from the so-called "faint supernovae" or "mixing-and-fallback" models with masses of ∼20–60 $M_{\odot}$ (e.g., Umeda & Nomoto 2003, 2005; Nomoto et al. 2013; Tominaga et al. 2014), or "spinstar" models with masses > 60–100 $M_{\odot}$ (Meynet et al. 2006, 2010; Chiappini 2013); (2) CEMP-*s* stars from binary mass transfer from intermediate-mass (1–4 $M_{\odot}$) AGB stars, which have now evolved to become faint white dwarfs (e.g., Suda et al. 2004; Herwig 2005; Lucatello et al. 2005; Komiya et al. 2007; Bisterzo et al. 2011; Hansen et al. 2015). The results from recently completed long-term radial-velocity monitoring programs (Starkenburg et al. 2014; Hansen et al. 2016a,b; Jorissen et al. 2016) provide strong support for these assertions, based on the very different binary fractions of these two subclasses of CEMP stars.

Since the proposed mass ranges for the progenitors of CEMP-no and CEMP-*s* differ substantially, the relative fractions of CEMP-no and CEMP-*s* stars between the IHP and OHP can potentially provide strong constraints on the initial mass functions (IMFs) in the environments that were dominantly responsible for the formation of the two populations, as suggested by a number of previous authors (e.g., Carollo et al. 2014; Lee et al. 2014, and references therein). The best surviving candidates for the environments in which early star formation took place (perhaps corresponding to the lower-mass mini-halos that contributed stars to the OHP) are the ultra-faint dwarf (UFD) galaxies around the MW discovered during the SDSS (e.g., Belokurov et al. 2006a,b; Zucker et al. 2006). It is presumably no coincidence that our substantially higher fraction of CEMP-no stars associated with the OHP, compared with the CEMP-*s* stars of the OHP, is consistent with the relative dominance of CEMP-no stars among the UFDs associated with the MW (e.g., Frebel et al. 2014). Indeed, the large fraction of CEMP-no stars we associate with the OHP suggests that systems similar to disrupted UFD galaxies may have contributed significantly to the formation of the OHP of the MW.

6. SUMMARY AND CONCLUSIONS

We have used a sample of over 100,000 MSTO stars from the SDSS to investigate the *in situ* spatial distribution of carbonicity ([C/Fe]) of the Galactic halo system, and demonstrated that it exhibits different levels of carbonicity as the distance from the Galactic plane increases. Dividing our sample into four regions in the plane of $|Z|$ vs. R, based on their carbon enhancement and location, we construct the MDF for each region. The MDFs of the halo regions are interpreted in terms of the differing contributions from the inner- and outer-halo populations. The IHP exhibits a peak at [Fe/H] $\sim$ –1.5, while a peak at [Fe/H] $\sim$ –2.2 is associated with the OHP, consistent with a number of previous studies. This result provides further evidence for the duality of the Galactic halo, based on an entirely different approach from the ones used before.

We have quantitatively assessed the relative fractions of CEMP-no and CEMP-*s* stars (classified on the basis of their derived absolute carbon abundances, A(C)) in the IHR and OHR (which we associate with dominant contributions from the IHP and OHP), and find that that the CEMP stars in the OHR exhibit a significantly higher proportion of CEMP-no stars relative to CEMP-*s* stars than found for the CEMP stars in the IHR.

The different MDFs and CEMP-no/CEMP-*s* fractions between the stars we associate with the IHP and OHP suggest that these individual halo components have received contributions of the nucleosynthesis products from different astrophysical progenitors, and experienced different assembly histories. Ultimately, this information can be used to constrain the mass distributions of the mini-halos from which they formed, as well as their star-formation histories.

We are currently exploring maps of the spatial distributions for larger samples of CEMP-no and CEMP-*s* stars, based on their identification from the Yoon–Beers diagram of A(C) vs. [Fe/H] (Figure 1 of Yoon et al. 2016), drawing on both the SDSS and the Large Sky Area Multi-Object Fiber Spectroscopic Telescope (LAMOST; Cui et al. 2012) surveys. Such maps can be compared with current and future numerical simulations of the formation of the halo of the MW. A new analysis of the kinematics for much larger samples of CEMP-no and CEMP-*s* stars than previously considered, based on more recent high- and medium-resolution spectroscopic analyses, is also now underway, and should prove illuminating.

We thank an anonymous referee for his/her careful review of this manuscript, and for pointing out a number of places where we could improve the clarity of the presentation.

Funding for SDSS-III has been provided by the Alfred P. Sloan Foundation, the Participating Institutions, the National Science Foundation, and the U.S. Department of Energy Office of Science. The SDSS-III Web site is http://www.sdss3.org/.

SDSS-III is managed by the Astrophysical Research Consortium for the Participating Institutions of the SDSS-III Collaboration including the University of Arizona, the Brazilian Participation Group, Brookhaven National Laboratory, University of Cambridge, Carnegie Mellon University, University of Florida, the French Participation Group, the German Participation Group, Harvard University, the Instituto de Astrofisica de Canarias, the Michigan State/Notre Dame/JINA Participation Group, Johns Hopkins University, Lawrence Berkeley National Laboratory, Max Planck Institute for Astrophysics, Max Planck Institute for Extraterrestrial Physics, New Mexico State University, New York University, Ohio State University, Pennsylvania State University, University of Portsmouth, Princeton University, the Spanish Participation Group, University of Tokyo, University of Utah, Vanderbilt University, University of Virginia, University of Washington, and Yale University.

This work was supported by the 2014 research fund of Chungnam National University. Y.S.L. also acknowledges partial support from the National Research Foundation of Korea to the Center for Galaxy Evolution Research and Basic Science Research Program through the National Research Foundation of Korea (NRF) funded by the Ministry of Science, ICT and Future Planning (NRF-2015R1C1A1A02036658). T.C.B., V.P., J.Y., and D.C. acknowledge partial support for this work from grants PHY 08-22648: Physics Frontier Center/Joint Institute of Nuclear Astrophysics (JINA), and PHY 14-30152: Physics Frontier Center/JINA Center for the Evolution of the Elements (JINA-CEE), awarded by the US National Science Foundation. T.M. acknowledges support by the European Union FP7 programme through ERC grant number 320360. This work benefited from support by the US National Science Foundation under Grant No. PHY 14-30152 (JINA Center for the Evolution of the Elements).

REFERENCES

Alam, S., Albareti, F. D., Allende Prieto, C., et al. 2015, ApJS, 219, 12
Allende Prieto, C., Sivarani, T., Beers, T. C., et al. 2008, AJ, 136, 2070
Allende Prieto, C., Fernandez-Alvar, E., Schlesinger, K. J., et al. 2014, A&A, 568, 7
An, D., Beers, T. C., Johnson, J. A., et al. 2013, ApJ, 763, 65
An, D., Beers, T. C., Santucci, R. M., et al. 2015, ApJ, 813, L28
Aoki, W., Beers, T. C., Christlieb, N., Norris, J.E., Ryan, S. G., & Tsangarides, S. 2007, ApJ, 655, 492
Asplund, M., Grevesse, N., Sauval, A. J., & Scott, P. 2009, ARA&A, 47, 481
Beers, T. C., Chiba, M., Yoshii, Y., et al. 2000, AJ, 119, 2866
Beers, T. C., & Christlieb, N. 2005, ARA&A, 43, 531
Beers, T. C., Carollo, D., Ivezić, Ž., et al. 2012, ApJ, 746, 34
Beers, T. C., Placco, V. M., Carollo, D., et al. 2016, ApJ, in press (arXiv:1611.03762)
Belokurov, V., Zucker, D. B., Evans, N. W., et al. 2006a, ApJ, 642, L137
Belokurov, V., Zucker, D. B., Evans, N. W., et al. 2006b, ApJ, 647, L111
Bisterzo, S., Gallino, R., Straniero, O., Cristallo, S., & Käppeler, F. 2011, MNRAS, 418, 284
Carney, B. W., Latham, D. W., Stefanik, R. P., et al., 2003, AJ, 125, 293
Carollo, D., Beers, T. C., Lee, Y. S., et al. 2007, Nature, 450, 1020
Carollo, D., Beers, T. C., Chiba, M., et al. 2010, ApJ, 712, 692
Carollo, D., Beers, T. C., Bovy, J., et al. 2012, ApJ, 744, 195
Carollo, D., Freeman, K., Beers, T. C., et al. 2014, ApJ, 788, 180
Chen, Y. Q., Zhao, G., Carrell, K., et al. 2014, ApJ, 795, 52
Chiappini, C. 2013, AN, 334, 5951
Cui, X. Q., Zhao, Y. H., Chu, Y. Q, et al. 2012, RAA, 12, 1197
Das, P., & Binney, J. 2016, MNRAS, 460, 1725
Dawson, K. S., Schlegel, D. J., Ahn, C., et al. 2013, AJ, 145, 10
de Jong, J. T. A., Yanny, B., Rix, H.-W., et al. 2010, ApJ, 714, 663
Fernandez-Alvar, E., Allende Prieto, C., Schlesinger, K. J., et al. 2015, A&A, 577, 81
Fernandez-Alvar, E., Allende Prieto, C., Beers, T. C., Lee, Y. S., Masseron, T., & Schneider, D. P. 2016a, A&A, 593, 28
Fernandez-Alvar, E., Carigi, L., Allende Prieto, C., et al. 2017, MNRAS, 465, 1586
Frebel, A., Christlieb, N., Norris, J. E., et al. 2006, ApJ, 652, 1585
Frebel, A., Simon, J. D., & Kirby, E. N. 2014, ApJ, 786, 74
Font, A. S., McCarthy, I. G., Crain, R. A., et al. 2011, MNRAS, 416, 2802
Gaia Collaboration, Brown, A. G. A., Vallenari, A., et al. 2016, A&A, 595, 2
Hampel, M., Stancliffe, R. J., Lugaro, M., & Meyer, B. S. 2016, ApJ, 831, 171
Hansen, T. T., Hansen, C. J., Christlieb, N., et al. 2015, ApJ, 807, 173
Hansen, T. T., Andersen, J., Nordström, B., et al. 2016a, A&A, 586, 160
Hansen, T. T., Andersen, J., Nordström, B., et al. 2016b, A&A, 588, 3
Hattori, K., Yoshii, Y., Beers, T. C., Carollo, D., & Lee, Y. S. 2013, ApJ, 763, L17
Helmi, A., Veljanoski, J., Breddels, M. A., Tian, H., & Sales, L. V. 2017, A&A, in press (arXiv:1611.00222)
Herwig, F. 2005, ARA&A, 43, 435
Ivezić, Ž., Sesar, B., Jurić, M., et al. 2008, ApJ, 684, 287
Janesh, W., Morrison, H. L., Ma, Z., et al. 2016, ApJ, 816, 80
Jorissen, A., Van Eck, S., Van Winckel, H., et al. 2016, A&A, 586, A158
Kinman, T. D., Cacciari, C., Bragaglia, A., Smart, R., & Spagna, A. 2012, MNRAS, 422, 2116
Komiya, Y., Suda, T., Minaguchi, H., et al. 2007, ApJ, 658, 367
Kunder, A., Kordopatis, G., Steinmetz, M., et al. 2016, AJ, submitted (arXiv:1609.03210)
Lee, Y. S., Beers, T. C., Sivarani, T., et al. 2008a, AJ, 136, 2022
Lee, Y. S., Beers, T. C., Sivarani, T., et al. 2008b, AJ, 136, 2050
Lee, Y. S., Beers, T. C., Allende Prieto, C., et al. 2011, AJ, 141, 90
Lee, Y. S., Beers, T. C., Masseron, T., et al. 2013, AJ, 146, 132
Lee, Y. S., Suda, T., Beers, T. C., & Stancliffe, R. J. 2014, ApJ, 788, 131
Lucatello, S., Tsangarides, S., Beers, T. C., et al. 2005, ApJ, 625, 825
Lucatello, S., Beers, T. C., Christlieb, N. C., et al. 2006, ApJ, 652, L3
McCarthy, I. G., Font, A. S., Crain, R. A., et al. 2012, MNRAS, 420, 2245
Meynet, G., Ekström, S., & Maeder, A.. 2006, A&A, 447, 623
Meynet, G., Hirschi, R., Ekstrom, S., et al. 2010, A&A, 521, 30
Monachesi, A., Bell, E. F., Radburn-Smith, D. J., et al. 2016, MNRAS, 457, 1419
Newberg, H. J., Yanny, B., Rockosi, C., et al. 2002, ApJ, 569, 245
Nomoto, K., Kobayashi, C., & Tominaga, N. 2013, ARA&A, 51, 457
Placco, V. M., Frebel, A., Beers, T. C., Stancliffe, R. J. 2014 ApJ, 797, 21
Placco, V. M., Beers, T. C., Reggiani, H., & Meléndez, J., 2016 ApJ, 829, L24

Schönrich, R., Asplund, M., & Casagrande, L. 2011, MNRAS, 415, 3807
Smolinski, J. P., Lee, Y. S., Beers, T. C., et al. 2011, AJ, 141, 89
Starkenburg, E., Shetrone, M. D., McConnanchie, A. W., & Venn, K. A. 2014, MNRAS, 441, 1217
Suda, T., Aikawa, M., Machida, M. N., & Fujimoto, M. Y. 2004, ApJ, 611, 476
Tissera, P. B., White, S. D. M., & Scannapieco, C. 2012, MNRAS, 420, 255
Tissera, P. B., Scannapieco, C., Beers, T. C., & Carollo, D. 2013, MNRAS, 432, 3391
Tissera, P. B., Beers, T. C., Carollo, D., & Scannapieco, C. 2014, MNRAS, 439, 3128
Tominaga, N., Iwamoto, N., & Nomoto, K. 2014, ApJ, 785, 98
Umeda, H., & Nomoto, K. 2003, Nature, 422, 871
Umeda, H., & Nomoto, K. 2005, ApJ, 619, 427
Yanny, B., Newberg, H. J., Johnson, J. A., et al. 2009, AJ, 137, 4377
Yong, D., Norris, J. E., Bessell, M. S., et al. 2013, ApJ, 762, 27
Yoon, J., Beers, T. C., Placco, V. M., et al. 2016, ApJ, in press (arXiv:1607.06336)
York, D. G., Adelman, J., Anderson, J. E., Jr., et al. 2000, AJ, 120, 1579
Zolotov, A., Willman, B., Brooks, A. M., et al. 2009, ApJ, 702, 1058
Zucker, D. B., Belokurov, V., Evans, N. W., et al. 2006, ApJ, 643, L103